

SEARCHING FOR BALMER-DOMINATED TYPE IA SUPERNOVA REMNANTS IN M33

CHRIS DING-JYUN LIN (林鼎鈞)

Institute of Astronomy and Astrophysics, Academia Sinica, No.1, Sec. 4, Roosevelt Rd., Taipei 10617, Taiwan, R.O.C.
djlin@asiaa.sinica.edu.tw and
Department of Physics, National Taiwan University, Taipei 10617, Taiwan, R.O.C.

YOU-HUA CHU (朱有花)

Institute of Astronomy and Astrophysics, Academia Sinica, No.1, Sec. 4, Roosevelt Rd., Taipei 10617, Taiwan, R.O.C.
yhchu@asiaa.sinica.edu.tw and
Department of Physics, National Taiwan University, Taipei 10617, Taiwan, R.O.C.

PO-SHENG OU (歐柏昇)

Institute of Astronomy and Astrophysics, Academia Sinica, No.1, Sec. 4, Roosevelt Rd., Taipei 10617, Taiwan, R.O.C.
psou@asiaa.sinica.edu.tw and
Department of Physics, National Taiwan University, Taipei 10617, Taiwan, R.O.C.

CHUAN-JUI LI (李傳睿)

Institute of Astronomy and Astrophysics, Academia Sinica, No.1, Sec. 4, Roosevelt Rd., Taipei 10617, Taiwan, R.O.C.
cjli@asiaa.sinica.edu.tw
Draft version September 15, 2020

ABSTRACT

We have searched for Balmer-dominated Type Ia SNRs in M33 by selecting thermal X-ray sources with $L_X \geq 5 \times 10^{35}$ ergs s^{-1} , identifying associated $H\alpha$ emission features, and checking their [S II] and [O III] emission properties. Our search did not find any Balmer-dominated Type Ia SNRs in M33. This result is puzzling because M33 is 2–3 times more massive than the LMC, yet the LMC hosts five Balmer-dominated Type Ia SNRs and M33 has none. We have considered observational biases, interstellar densities and ionization conditions, Type Ia SN rate expected from the star formation history and Type Ia SN delay time distribution function, and metallicity effect. None of these can explain the absence of X-ray-bright Balmer-dominated Type Ia SNRs in M33. It is intriguing that the Galaxy has X-ray-bright and thermal Type Ia SNRs (Kepler and Tycho) as well as X-ray-faint and nonthermal Type Ia SNRs (G1.9+0.3, SN1006, and RCW86), while the LMC does not have the X-ray-faint and nonthermal ones and M33 does not have the X-ray-bright and thermal ones.

Subject headings: galaxies: individual (M33) — galaxies: ISM — ISM: supernova remnants

1. INTRODUCTION

Type Ia supernovae (SNe) are recognized to originate from white dwarfs (WDs) in binary systems (Whelan & Iben 1973; Nomoto 1982; Webbink 1984); however, it is not known whether the binary companion is another WD or a normal star. If a surviving companion can be identified for a Type Ia SN, the nature of its progenitor can be affirmed.

Surviving companions have been searched for in young Type Ia supernova remnants (SNRs) because they have not moved far from the sites of SN explosion and would be easier to find. A handful of young Type Ia SNRs are known in the Galaxy (such as Tycho, Kepler, G1.9+0.3, SN1006, and RCW86) and the Large Magellanic Cloud (LMC; 0509–67.5, 0519–69.0, 0548–70.4, DEM L71, and N103B), but no surviving companions of their SN progenitors have been unambiguously identified and confirmed (e.g., Ruiz-Lapuente et al. 2004, 2018; González Hernández et al. 2009, 2012; Schaefer & Pagnotta 2012; Edwards et al. 2012; Kerzendorf et al. 2013, 2014; Pagnotta & Schaefer 2015; Li et al. 2017, 2019; Litke et al. 2017; Kerzendorf et al. 2018).

To enlarge the sample of young Type Ia SNRs, we in-

tend to search for them in the spiral galaxy M33 at a distance of 820 kpc (Freedman et al. 2001), or a distance modulus (DM) of 24.6. For such a distance, the currently being constructed 30m-class optical telescopes will be able to detect surviving companions of SN progenitors in the future.

Young Type Ia SNRs can be identified by their Balmer-dominated optical spectra produced by collisionless shocks moving into a partially neutral ambient medium (Chevalier et al. 1980). Such Balmer-dominated spectra are not associated with core-collapse (CC) SNRs because their surrounding interstellar gas has been photoionized by either their massive progenitors or nearby massive stars. For Balmer-dominated Type Ia SNRs, the ionization fraction of their ambient medium is lower and can be used to constrain properties of their SN progenitors (Woods et al. 2018). The Type Ia nature of Balmer-dominated SNRs has been definitively confirmed through spectroscopic observations of the light echos of their SNe (e.g., Krause et al. 2008; Rest et al. 2008), or X-ray spectral analyses of their SN ejecta abundances that are consistent with the nucleosynthesis yields of Type Ia SNe (e.g., Hughes et al. 1995; Badenes et al. 2006, 2008).

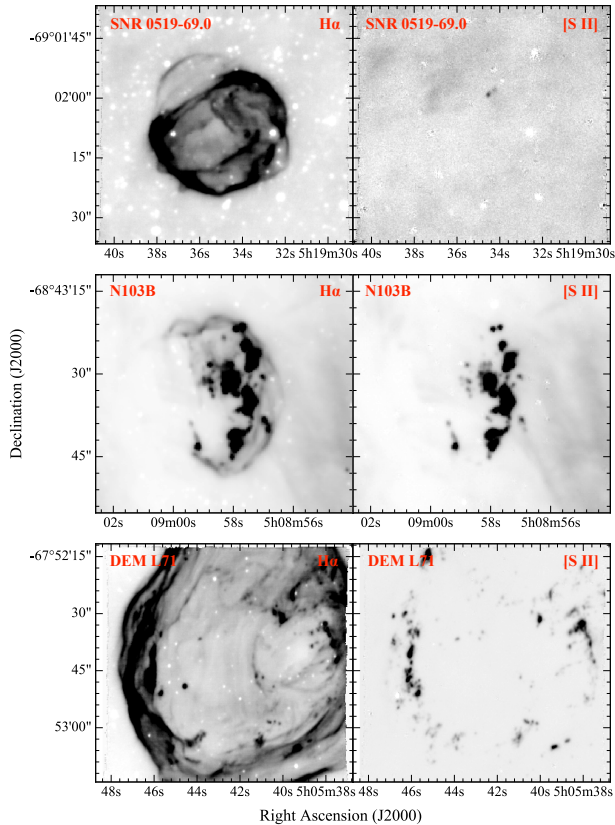


FIG. 1.— $H\alpha$ and $[S\ II]$ images of Balmer-dominated SNRs 0519–69.0, N103B, and DEM L71 extracted from VLT MUSE observations (Li et al. 2020, in preparation). The SNR names are marked in the top left corner of the left panels and the filters are marked in the upper right corner of each panel. Note that the Balmer-dominated shells disappear in the $[S\ II]$ images completely. Only dense knots are visible in the $[S\ II]$ images.

Balmer-dominated young Type Ia SNRs are characterized by a Balmer shell, of which the $[S\ II]$ emission is not detected, with $[S\ II]/H\alpha$ ratios well below 0.05, and the $[O\ III]$ emission may be detected with $[O\ III]/H\beta$ ratios of 0.005–0.015; however, these SNRs may contain dense knots where the electron densities can be over 1000 cm^{-3} and $[S\ II]/H\alpha$ ratios may range from 0.1 to 0.7 (Li et al. 2020, in preparation). The Balmer shells and dense knots are illustrated in three example LMC SNRs in Figure 1.

The identification of Balmer-dominated SNRs in galaxies beyond the LMC becomes tricky because the Balmer shell and the imbedded dense knots may not be resolved. Conventional optical surveys of extragalactic SNRs using the selection criterion of integrated $[S\ II]/H\alpha$ ratio greater than a threshold of 0.4 or higher (e.g., Matonick & Fesen 1997) would have missed Balmer-dominated SNRs. This is the case for optical SNR surveys in M33 (Gordon et al. 1998; Lee & Lee 2014). Thus, we have to make a new search for young Balmer-dominated Type Ia SNRs in M33 employing a different methodology.

Using the X-ray and optical properties of Balmer-dominated Type Ia SNRs in the LMC as a template, as shown in Table 1, we examined optical counterparts of all thermal X-ray sources that have X-ray luminosity greater than $5 \times 10^{35}\text{ erg s}^{-1}$ in M33, but did not find any Balmer-dominated Type Ia SNRs. This result is puzzling because M33 is more massive than the LMC

and we expect proportionally more Type Ia SNRs.

This paper reports our search for Balmer-dominated Type Ia SNRs in M33. The search methodology is described in Section 2, the results are presented in Section 3, the SNRs are individually analyzed in Section 4, and the implications of the results are discussed in Section 5. A brief summary and conclusion is given in Section 6.

2. METHODOLOGY

To search for young Balmer-dominated Type Ia SNRs in M33, we use known objects in the LMC as templates (see Table 1). We first use an X-ray luminosity threshold to select X-ray sources that are as luminous as the Balmer-dominated Type Ia SNRs in the LMC. We further require their X-ray spectral properties to be consistent with those of thermal plasma emission in order to filter out X-ray binaries (XRBs), pulsar wind nebulae (PWNe) and active galactic nuclei (AGNs). For the selected luminous thermal X-ray sources, we examine their optical counterparts, search for nebular shells in $H\alpha$ images and check $[O\ III]$ and $[S\ II]$ images for forbidden line emission. A luminous thermal X-ray source coincident with an $H\alpha$ shell without counterparts in forbidden lines would be a promising candidate for Balmer-dominated Type Ia SNR.

2.1. X-ray Luminosity of Young Type Ia SNRs

The LMC hosts five Balmer-dominated Type Ia SNRs. The first four were reported by Tuohy et al. (1982): 0509-67.5, 0519-69.0, DEM L71, and 0548-70.4. The latter two are larger and show traces of forbidden line emission, which has been interpreted to be caused by an age effect, as the post-shock material gradually becomes collisionally ionized. The fifth, N103B, has a Balmer-dominated shell encompassing dense ionized knots of circumstellar medium (CSM) that emit bright forbidden lines. Examples of Balmer shells and dense knots of three LMC SNRs are shown in Figure 1. The existence of dense CSM in a Type Ia SNR may imply that the WD progenitor had a normal star companion (Hachisu et al. 2008). The optical and X-ray sizes and X-ray luminosities (L_X) in the 0.3–2.1 keV band of these 5 Balmer-dominated Type Ia SNRs are given in Table 1. Their unabsorbed L_X versus size are plotted in Figure 2, where other LMC SNRs and Galactic young Type Ia SNRs are also included for comparisons (Ou et al. 2018). The L_X of the four smaller Balmer-dominated LMC SNRs are all greater than $10^{36}\text{ ergs s}^{-1}$, while the largest Balmer-dominated LMC SNR is fainter, with $L_X \sim 8 \times 10^{35}\text{ ergs s}^{-1}$. The small Galactic Type Ia SNRs appear to show two distinct categories: the X-ray-bright ones have mostly thermal emission with L_X greater than $10^{36}\text{ ergs s}^{-1}$, such as the Kepler and Tycho SNRs (Badenes et al. 2007), and the X-ray-faint ones have mostly nonthermal emission with L_X less than $2 \times 10^{35}\text{ ergs s}^{-1}$, such as G1.9+0.3, SN1006, and RCW86 (Reynolds et al. 2008; Koyama et al. 1995; Williams et al. 2011). The X-ray-bright ones are similar to those in the LMC, while the X-ray-faint ones do not have counterparts in the LMC. In this work, we use the criterion of $L_X \geq 5 \times 10^{35}\text{ ergs s}^{-1}$ to select candidates of X-ray-bright Balmer-dominated Type Ia SNRs in M33.

M33 has been observed by *Chandra X-ray Observatory* for a total of 1.4 Ms in the program ChASem33

TABLE 1
PROPERTIES OF BALMER-DOMINATED TYPE IA SNRS IN THE LMC

SNR	Optical size ^a (pc)	X-ray size ^b (pc)	L_X (0.3–2.1keV) ^b (10^{36} ergs s ⁻¹)	kT ^b (keV)	[S II]/H α ^c
0509–67.5	7.8×7.1	8.0×7.5	3.4	0.3	<0.02
0519–69.0	9.7×8.3	8.4×8.1	10.6	0.4, 0.6	<0.03
DEM L71	23×17	21×18	7.7	0.2, ~0.8	~0.1
0548–70.4	28×25	29×26	0.8	0.6	...
N103B	7.7×6.2	7.5×7.4	16.7	~ 1	0.1–0.2

NOTE. —

^a Measured from *HST* images, adopting $1'' = 0.25$ pc for the LMC.

^b X-ray size, luminosity L_X , and plasma temperature kT are from Chandra Supernova Remnant Catalog (https://hea-www.harvard.edu/ChandraSNR/snrcat_lmc). The plasma temperature is for the bulk soft X-ray emission that includes the Fe L-shell lines. The plasma temperature of N103B is from Lewis et al. (2003).

^c Integrated over the entire SNR. From Li et al. 2020, in preparation. The background diffuse ISM emission has high [S II]/H α ratios, and a highly non-uniform background causes large uncertainty in the measurements.

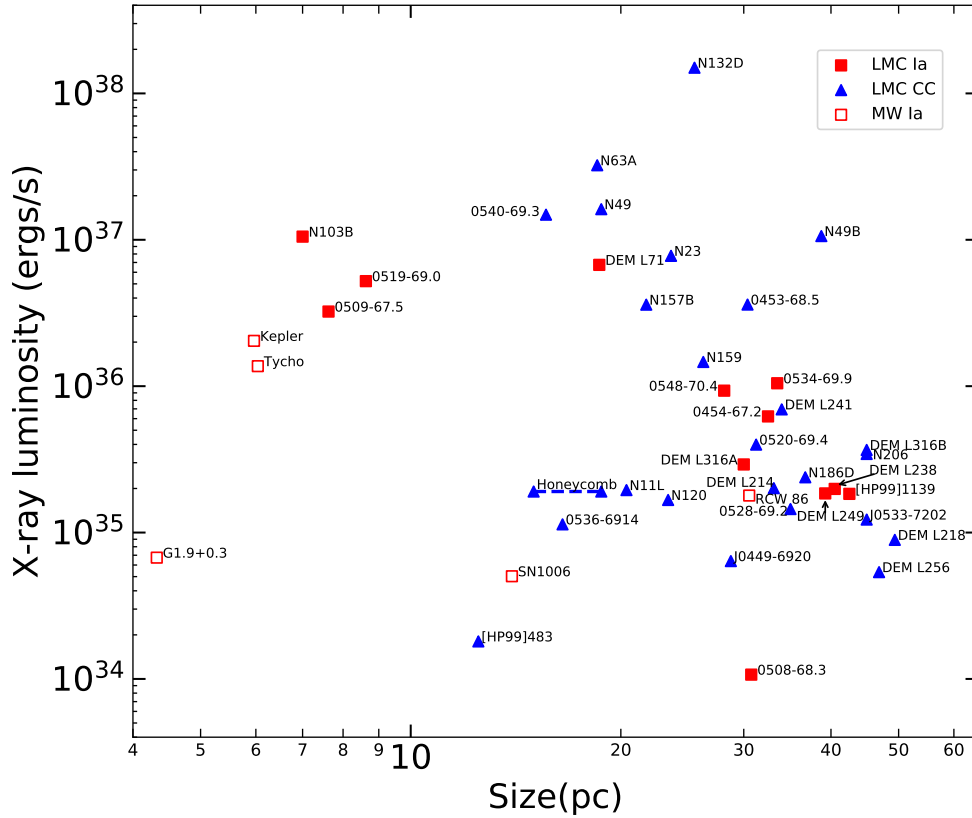


FIG. 2.— X-ray luminosity versus size plot for LMC SNRs, reproduced from Ou et al. (2018). Young Type Ia SNRs in the Milky Way galaxy are also included in this plot for comparison. The core-collapse (CC) SNRs are plotted in triangles, and the Type Ia SNRs in squares, with filled symbols for the LMC and open symbols for the Milky Way. SNRs greater than 50 pc in diameter are not included in this plot.

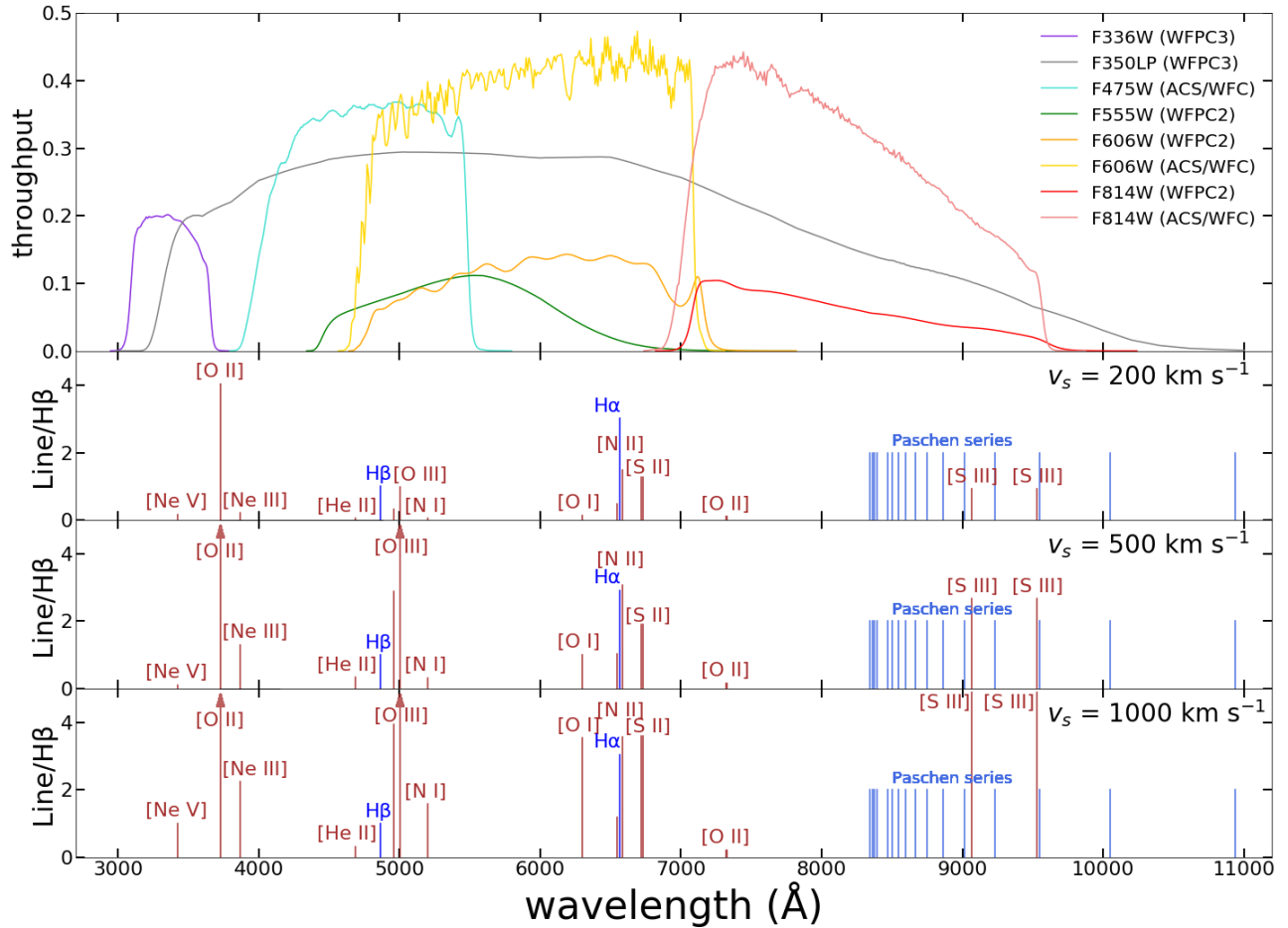


FIG. 3.— *HST* filter profiles and stronger emission lines for shock components of solar abundance model from Allen et al. (2008) with shock velocity $v_s = 200, 500, 1000 \text{ km s}^{-1}$. The emission lines which have an arrow on their top indicate their line strengths are out of scale.

(Tüllmann et al. 2011). These ACIS-I observations cover about 70% of the central area of radius ~ 4 kpc, and can detect sources with $L_X > 4 \times 10^{34}$ ergs s^{-1} in the 0.5–2.0 keV band. The brightest sources have adequate counts in at least 8 spectral bins to allow meaningful spectral fits to determine L_X , and the best-fit results are reported in Table 9 of Tüllmann et al. (2011). They have considered two spectral models: power-law for nonthermal sources and vpec (Variable abundance Astrophysical Plasma Emission Code) for thermal plasma sources. To search for X-ray-bright Balmer-dominated Type Ia SNRs, we have selected all thermal X-ray sources whose vpec model fits indicate unabsorbed $L_X \geq 5 \times 10^{35}$ ergs s^{-1} . Twenty-one sources meet these selection criteria.

2.2. Balmer-dominated Shell-like Structure

Balmer-dominated Type Ia SNRs in the LMC all exhibit a shell-like structure in $H\alpha$ images, and the $H\alpha$ shells essentially disappear in [S II] $\lambda\lambda 6716, 6731$, and [O III] $\lambda 5007$ images, as illustrated in Figure 1. This contrast can be explained by collisionless shocks advancing into a partially neutral medium, where the [O III] and [S II] line emission is expected to be 10–100 times fainter than the $H\alpha$ emission (Chevalier et al. 1980).

We have used the $H\alpha$, [S II], and [O III] images obtained with the Mosaic CCD camera on the Mayall 4-m Telescope at the Kitt Peak National Observatory (KPNO) on 2000 October 5 by Massey et al. (2007). Their M33-Center field, centered at 01h33m50.90s, $+30^\circ 39' 37''.0$ with a $36' \times 36'$ field of view, covers all the *Chandra* X-ray sources that have thermal plasma-emission in M33. Each line image was taken with a filter of ~ 50 Å width, and five 300 s exposures dithered to compensate CCD gaps. The $H\alpha$ image is used to search for shell structure associated with the X-ray source and the [O III] and [S II] images are used to check their forbidden line emission.

At the distance of M33, $1''$ corresponds to roughly 4 pc, and ground-based images with $\sim 1''$ seeing are inadequate to resolve the SNR shells. We have thus searched for archival *Hubble Space Telescope* (*HST*) images of M33 to complement the above-mentioned 4-m Mosaic CCD images. In the entire M33 galaxy, *HST* $H\alpha$ and forbidden line images are available only for the area centered on the giant H II region NGC 604. For the other regions in M33, only broad-band images are available. The *HST* broad-band filters often cover bright nebular lines as illustrated in Figure 3, where the filter response curves are plotted in the top panel and modeled nebular lines for 1000, 500, and 200 km s^{-1} shocks (Allen et al. 2008) are plotted in the lower three panels, respectively. It may be possible to see nebular emission in broad-band images. We have thus retrieved archival *HST* broad-band images to search for nebular emission to examine SNR morphologies at $0''.1$ resolution. These will be included in our discussion of individual SNRs.

3. NATURE OF THE BRIGHTEST THERMAL X-RAY SOURCES PROJECTED IN M33

In the final source catalog of ChASeM33 (Tüllmann et al. 2011), the 21 brightest thermal X-ray sources have $L_X \geq 5 \times 10^{35}$ ergs s^{-1} . Table 2 lists their source No., source ID, absorption column densities, plasma tem-

peratures, L_X , other names, identifications of their nature, detection in forbidden line images, and optical sizes. Among these 21 sources, nine are associated with known SNRs (Long et al. 2010; Lee & Lee 2014). These SNRs are individually discussed in Section 4. We have also examined the other 12 sources in detail. As described below, we confirm 5 foreground stars (FSs) in the Galaxy, suggest 2 high-mass X-ray binaries (HMXBs) in M33, and comment on the other 5 sources. The plasma temperature distributions of these different categories of objects are shown in Figure 5. It is clear from this temperature distribution that the unidentified sources are unlikely to be SNRs because their plasma temperatures are too high.

3.1. Foreground Stars

Five of these 21 brightest thermal X-ray sources, No. 279, 287, 301, 462, and 585, are associated with known FSs (Tüllmann et al. 2011). The parallaxes of four of these stars can be found in the Gaia data release 2 (DR2, Gaia Collaboration et al. 2018) to confirm their being in the solar neighborhood. Their spectral types and origins of X-ray emission can be assessed from their photometric measurements, assuming negligible extinction and comparing them with those of main sequence stars compiled in Table 5 of Pecaut & Mamajek (2013).

Source 279's stellar counterpart has $V = 17.3$, $B - V = 1.73$, $V - R = 1.37$ (Massey et al. 2006, 2007, 2016), and $H - K = 0.308$ (Cutri et al. 2003). Gaia DR2 reports a parallax of 10.789 ± 0.129 mas, or a distance of 93 ± 1 pc. Both the absolute magnitude and colors of this star are consistent with those of a main sequence M4–M5 star. Its L_X/L_{bol} is $\sim 4 \times 10^{-4}$, consistent with the stellar coronal origin of the X-ray emission (Fleming et al. 1995; Zickgraf et al. 2005). This X-ray source has also been marked as variable by Tüllmann et al. (2011).

Source 287's stellar counterpart was not reported by Massey et al. (2006, 2007, 2016). Other catalogs report $V = 11.4$, $B - V = 0.37$ to 0.43 , $V - R = 0.25$ to 0.67 , $V - I = 1.22$ (Zacharias et al. 2004; Ivanov 2008; Bourges et al. 2014), $J - H = 0.34$ and $H - K = 0.11$ (Cutri et al. 2003). The large $V - R$ differences between observations made by different people at different epochs indicate that this star might be variable or have an eclipsing companion. No main sequence stars can meet the observed colors from blue to near-IR wavelengths. The $B - V$ and $V - R$ colors suggest a main sequence spectral type of F2–F5 V; however, the $V - I$ color suggests K5 V. Gaia DR2 reports a parallax of 5.224 ± 0.067 mas, or a distance of 191 ± 3 pc. An F2–F5 V star at such a distance would have $V \sim 10$, brighter than the observed 11.4. We conclude that the stellar counterpart of Source 287 is a foreground star, but it is not a single main sequence star.

Source 301 has two stars projected within $3''$. The star nearest to the X-ray position is also brighter, thus we take this star as the optical counterpart. It has $V = 14.4$, $B - V = 1.08$, $V - R = -0.27$, and $U - B = 1.03$ (Massey et al. 2006, 2007, 2016), or $V = 13.89$, $B - V = 1.25$ and $V - R = 0.465$ (Qi et al. 2015), and $J - H = 0.58$, $H - K = 0.08$ (Cutri et al. 2003). The optical colors and magnitudes reported by the two groups are significantly different; for example, the $V - R$ color even changed sign between the two measurements. The colors reported by Massey et al. correspond to $\sim K4$ V, if the anomalous $V -$

TABLE 2
21 BRIGHTEST THERMAL X-RAY SOURCES IN M33

No. ^a	Source ID ^a	N_{H}^b (10^{22} cm ⁻²)	kT^c (keV)	$L_{\text{X}}(0.35\text{-}2\text{ keV})^a$ (10^{35} ergs s ⁻¹)	Other Names ^d (L10; LL14)	Identification ^e	Detection ^f	Optical Size (pc)
68	013303.55+303903.8	0.42	3.75	8.3	...	HMXB	[SII], [OIII]	...
100	013311.09+303943.7	0.01	0.55	5.2	023; 035	SNR	[SII], [OIII]	33×27
102	013311.75+303841.5	0.01	0.55	110.6	025; 037	SNR	[SII], [OIII]	21
184	013329.04+304216.9	0.01	0.56	19.4	036; 061	SNR	[SII], [OIII]	18×11
188	013329.45+304910.7	0.01	0.56	10.8	037; 062	SNR	[SII], [OIII]	34
197	013331.25+303333.4	0.01	0.60	24.0	039; 067	SNR	[SII], [OIII]	28×24
236	013335.90+303627.4	0.01	0.77	8.0	045; 074	SNR	[SII], [OIII]	48×30
245	013337.08+303253.5	1.78	0.16	112.1	046; 076	SNR	[SII], [OIII]	45×36
279	013341.90+303848.8	0.01	0.74	12.9	...	FS (M4–5 V)	[SII], [OIII]	...
287	013343.39+304630.6	0.01	0.48	11.9	...	FS (F2–5 V?)	[SII], [OIII]	...
301	013346.81+305452.8	1.51	1.05	16.5	...	FS (K1–6 V)	[SII], [OIII]	...
320	013352.12+302706.5	0.04	4.67	8.9	...	HMXB	[SII], [OIII]	...
334	013354.91+303310.9	0.01	0.44	20.4	071; 107	SNR	[SII], [OIII]	21
427	013410.69+304224.0	0.01	0.31	11.8	096; 140	SNR	[SII], [OIII]	22
450	013416.76+305101.8	0.68	4.34	5.6	...	NOC
462	013418.22+302446.1	0.29	0.81	6.7	...	FS (K6 V)	[SII], [OIII]	...
470	013421.09+304932.3	4.84	2.19	17.9	...	NOC
528	013432.02+303454.1	3.02	10.87	20.7	...	NOC
585	013444.23+304920.3	0.48	0.72	9.1	...	FS (M4 V)	[SII], [OIII]	...
587	013444.62+305535.0	0.97	3.58	24.5	...	HMXB?	[SII]	...
608	013451.10+304356.7	0.85	2.52	5.4	...	NOC

NOTE. —

^{a,b,c} From ChASem33 by Tüllmann et al. (2011).

^b Column density internal to M33.

^c Plasma temperatures.

^d L10-nnn denotes SNRs from Long et al. (2010), L14-nnn denotes SNRs from Lee & Lee (2014).

^e Physical nature of the source concluded in this paper. SNR – Supernova Remnant; HMXB – High Mass X-ray Binary; NOC – No Optical Counterpart; FS – Foreground Star with spectral type given in parentheses.

^f Detection in forbidden line images. Note that stellar continuum of bright stars can also be detected.

R is discarded. Qi et al. (2015) only has three passbands and thus the implied spectral type has a larger range of uncertainty, K1–K6 V. Assuming a K4 main sequence star, its $V = 13.9\text{--}14.4$ implies a distance of 310–240 pc and $L_{\text{X}}/L_{\text{bol}} \sim 2.0\text{--}1.3 \times 10^{-4}$, also consistent with a stellar coronal origin of the X-ray emission. Gaia DR2 did not provide a parallax for this star.

Source 462's stellar counterpart has $V = 16.49$, $B - V = 1.24$, $V - R = 0.74$, and $R - I = 0.74$, (Massey et al. 2006, 2007, 2016). These colors and magnitudes are consistent with a K6 V star at a distance of ~ 500 pc. Gaia DR2 reports a parallax of 1.183 ± 0.060 mas, or a distance of 845 ± 43 pc, and an effective temperature (T_{eff}) of 4372 K for this star. This T_{eff} is consistent with a K6 V star. Using the photometric distance, we obtain $L_{\text{X}}/L_{\text{bol}} \sim 4 \times 10^{-4}$, consistent with a stellar coronal origin of the X-ray emission. If the Gaia parallax is used, $L_{\text{X}}/L_{\text{bol}}$ would be $\sim 1 \times 10^{-3}$, on the high side of the possible range.

Source 585 has two stars projected within $2''$. Star 1 is closer, within $0''.5$, and fainter with $V = 18.31$, $B - V = 1.66$, $V - R = 1.37$, and $R - I = 1.19$, while Star 2 is off by $1''.6$ and has $V = 13.81$, $B - V = 0.82$, $U - B = 0.47$, and $V - R = 0.42$ (Massey et al. 2006, 2007, 2016). The colors and magnitudes of Star 1 are suggestive of an M4 V star at a distance of ~ 130 pc, and Star 2 a K0 V at a distance of ~ 420 pc. If Star 1 is the only star responsible for the X-ray source, its $L_{\text{X}}/L_{\text{bol}}$ would be $\sim 4.6 \times 10^{-4}$, consistent with a stellar coronal origin of the X-ray emission. Its distance of 130 pc is much closer than the 500 pc that corresponds to its Gaia DR2 parallax of 1.979 ± 0.103 mas. The Gaia DR2 parallax for Star 2 is similar, 2.199 ± 0.024 mas. Even if Star 2 contributes to

the X-ray emission, the combined $L_{\text{X}}/L_{\text{bol}}$ is still a few times 10^{-4} , within the range of stellar coronal emission (Fleming et al. 1995; Zickgraf et al. 2005).

3.2. Candidates for High-Mass X-ray Binaries

Two of the 21 brightest thermal X-ray sources in M33, Sources 68 and 320, might be HMXBs in M33.

Source 68 has $V = 19.45$, $U - B = -0.60$, $B - V = 0.43$, $V - R = 0.38$, and $R - I = 0.60$ (Massey et al. 2006, 2007, 2016). The colors do not agree with any types of stars. At long wavelengths it appears red and at short wavelengths it appears blue. Given M33's DM of 24.6, Source 68's M_V would be -5.2 even without extinction correction. It is not red enough to be a red supergiant; thus, it must be an early-type massive star in M33. We suggest that this source is most likely an HMXB in M33. Its X-ray luminosity is also consistent with an HMXB on the faint end.

Source 320 has $V = 19.43$, $B - V = 0.35$, $U - B = -0.83$, $V - R = 0.263$, and $V - I = 0.79$ (Massey et al. 2006, 2007, 2016). It has also been reported to have $V = 18.49$, $B - V = 1.90$, and $V - R = -1.07$ (Qi et al. 2015). The discrepancy between these two sets of measurements suggests the source is variable, and the X-ray source is indeed reported to be variable (Tüllmann et al. 2011). Following the same arguments as for Source 68, we suggest that the optical counterpart of Source 320 corresponds to a massive early-type star, and that this source is also an HMXB on the faint end.

Note that the temperatures of the thermal plasma models for the above two sources are also significantly higher than those of stellar coronal emission (Figure 5).

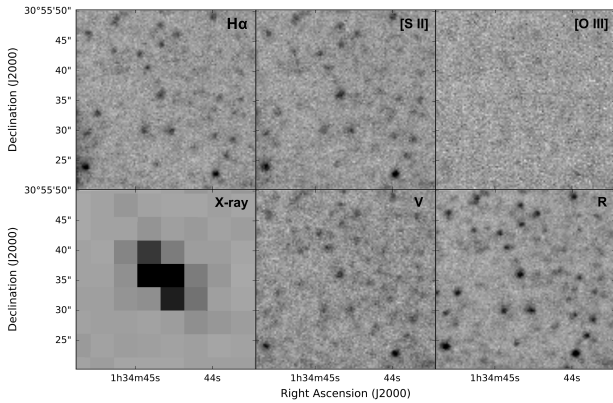


FIG. 4.— **No. 587, 013444.62+305535.0.** The top panels display $H\alpha$, $[S\ II]\ \lambda\lambda 6716, 6731$, and $[O\ III]\ \lambda 5007$ images taken with the Mosaic CCD camera on the KPNO 4-m telescope by Massey et al. (2007). The bottom panels show, from left to right, *Chandra* X-ray image (ObsID 2023, PI: Damiani), and KPNO 4-m Mosaic images in V and R . The possible optical counterpart is near the center of the field of view.

This lends further support to the HMXB explanation.

3.3. X-ray Sources without Optical Counterparts

Five of the 21 brightest thermal X-ray sources in M33, Sources 450, 470, 528, 587 and 608, do not have cataloged optical counterparts. We note that Source 587 may have an optical counterpart. This optical source, located at $\sim 1''.2$ from the X-ray source, is not cataloged by Massey et al. (2006, 2007, 2016) and must thus be fainter than $V = 19.5$. The X-ray source is located near the periphery of the *Chandra* observation’s field of view, where the point spread function deteriorates rapidly. As show in Figure 4, a faint point-like source projected near the centroid of the X-ray source is detected in the V , R , $H\alpha$, and $[S\ II]$, but not $[O\ III]$, images from Massey et al. (2007). The plasma temperature of this X-ray source is similar to that of Source 68, and its optical counterpart is somewhat fainter than the optical counterpart of Source 68. We suggest that Source 587 might also be a HMXB in M33, but this needs to be confirmed with better X-ray astrometry and optical photometric observations.

To assess possible nature of the other four bright X-ray sources, we plot a histogram of the distributions in the model-fit plasma temperature for SNRs, FSs, HMXB candidates, and unidentified objects (including source 587) in Figure 5. It is clear that all SNRs and foreground stars have low plasma temperatures, with the highest value at $kT = 1.05$ keV, while the HMXB candidates have kT around 4 keV. The five bright X-ray sources without confirmed optical counterparts all have kT greater than 2 keV. We suggest that these luminous X-ray sources without optical counterparts are background AGN or low-mass X-ray binaries in M33. If the optical counterpart of Source 587 can be confirmed, it will most likely be a HMXB.

4. ANALYSES OF INDIVIDUAL SUPERNOVA REMNANTS

For each SNR, we produce a six-panel figure to show its morphology in different wavelengths. The top three panels are $H\alpha$, $[S\ II]$, and $[O\ III]$ images taken with the KPNO 4-m telescope by Massey et al. (2007). The bottom row has an unfiltered *Chandra* X-ray image (ObsID

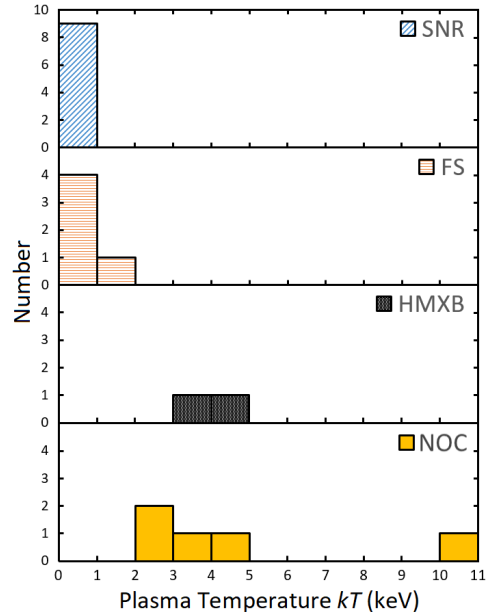


FIG. 5.— Plasma temperature distributions for the 21 brightest thermal X-ray sources in M33, plotted separately for confirmed SNRs, confirmed FSs, candidate HMXBs, and sources with no optical counterparts (NOC).

6383, PI: Sasaki) on the left, and two *HST* images taken with various filters from different programs. Information on the *HST* images are given in figure captions.

4.1. No. 100, 013311.09+303943.7 (L10-023, LL14-035)(Figure 6)

The X-ray image of this SNR shows a nice simple shell structure. The $H\alpha$ image shows a bright patch of emission along the shell rim in the southeast quadrant and fainter emission along the northern rim. The entire SNR is in the northwestern part of the large H II region NGC 592. The association with a star-forming complex suggests that the SN progenitor is most likely a massive star. The large variation of surface brightness along the shell rim is also consistent with what is observed in CC SNRs in the LMC (Ou et al. 2020, in preparation). The $[S\ II]$ and $[O\ III]$ images show a similar morphology of this SNR. The *HST* broad-band images have too short exposure times to be able to detect the nebular emission. We suggest that this is a CC SNR, definitely not a Balmer-dominated Type Ia SNR.

4.2. No. 102, 013311.75+303841.5 (L10-025)(Figure 7)

With an X-ray luminosity over 10^{37} ergs s^{-1} , this SNR is one of the two brightest X-ray-emitting SNRs in M33 (Tüllmann et al. 2011), and has thus been identified and well studied over the past two decades (Long et al. 1996; Gordon et al. 1998; Gaetz et al. 2007; Long et al. 2010; Lee & Lee 2014).

As analyzed and reported in detail by Gaetz et al. (2007), this SNR is projected against the H II region complex NGC 592, and its shell structure is well resolved by *Chandra* X-ray images. Figure 7 shows that the SNR shell is detected in $H\alpha$, $[S\ II]$, and $[O\ III]$ images as well, although the optical shell morphology does not follow the X-ray shell closely. The SNR is located on the western periphery of an $H\alpha$ arc and the bright eastern rim

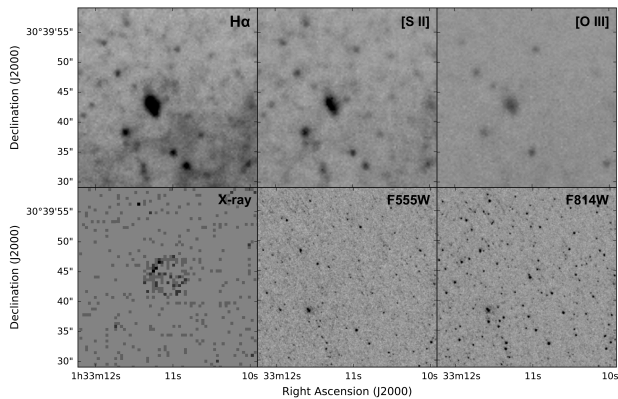


FIG. 6.— **No.100, 013311.09+303943.7 (L10-023)**. The *HST* images are taken with F555W (*V*) and F814W (*I*) filters in Program 11079 (PI: Bianchi).

of the X-ray shell abuts a dark cloud encompassed by the $H\alpha$ arc. It is possible that the bright X-ray emission is caused by the SNR shock running into the dense interstellar medium (ISM) near the molecular cloud (associated with the dark cloud). Figure 7 also shows three bright stellar sources to the northeast of the SNR, and the *HST* F555W and F814W images clearly resolve the middle source into two stars. The photometry of these stars reported by Massey et al. (2016) suggests that they are O supergiants. The stellar and interstellar environments of this SNR are closely associated with massive stars, suggesting a CC SN origin.

The most direct evidence of a SN’s origin is provided by the SN ejecta abundance determined from X-ray spectra (Hughes et al. 1995). The *Chandra* X-ray spectra reported by Gaetz et al. (2007) show significant oxygen emission in the 0.5–0.7 keV range relative to the iron emission peak. As the X-ray emission is distributed along the SNR shell rim, it most likely originates from the shock-heated ISM, rather than SN ejecta. Thus, the X-ray spectra cannot constrain the SN progenitor of this SNR.

In summary, we suggest that this SNR has a CC SN origin. While we cannot definitively exclude a Type Ia origin, the detection of [S II] and [O III] emission from the SNR clearly rejects it as a Balmer-dominated young Type Ia SNR nature.

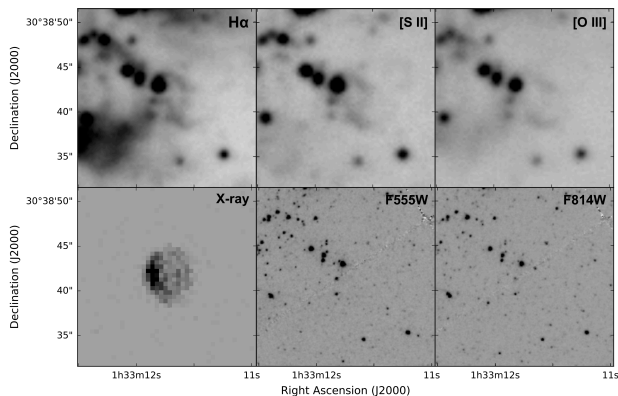


FIG. 7.— **No.102, 013311.75+303841.5 (L10-025)**. The *HST* images were taken with the F555W (*V*) and F814W (*I*) filters in Program 11079 (PI: Bianchi).

4.3. No.184, 013329.04+304216.9 (L10-036, LL14-061)(Figure 8)

This SNR was first identified from $H\alpha$ and [S II] images by Sabbadin & Bianchini (1979). Its elongated shape, 11 pc along east-west and 18 pc along north-south, is clearly visible in the $H\alpha$, [S II], and [O III] images (Figure 8). The *HST* F350LP and F336W (*U*) images have finally resolved the SNR shell, showing an opening to the east. In a large-scale environment, as shown in Figure 9, it can be seen that this SNR is projected within a large superbubble more than 200 pc in size. The active star-forming region is located at the southeast corner of the superbubble. The apparent association with a star-forming region may suggest that this SNR originates from a CC SN. However, the SNR’s shell morphology and large-scale environment are reminiscent of the Type Ia SNR N103B in the LMC (Li et al. 2017). We do not know whether this SNR is physically located within the superbubble or merely projected against it, as N103B viewed along the direction toward the superbubble around NGC 1850. Furthermore, the F350LP and F336W filters contain Balmer lines as well as forbidden lines, and it is not clear whether the Balmer lines and forbidden lines have different spatial distribution. As shown in Figure 1, some Balmer-dominated SNRs in the LMC do show knots of forbidden line emission with different spatial distribution from Balmer lines (Li et al. 2020, in preparation). See N103B in Figure 1 for an example and note the similarity in shell shape between SNR N103B and this SNR associated with Source 184. In summary, the apparent interstellar environment of this SNR suggests that it is likely of CC SN origin; however, high-resolution *HST* line images are needed to reveal the spatial distributions of Balmer and forbidden lines to conclude definitively whether there is a Balmer-dominated shell in this SNR.

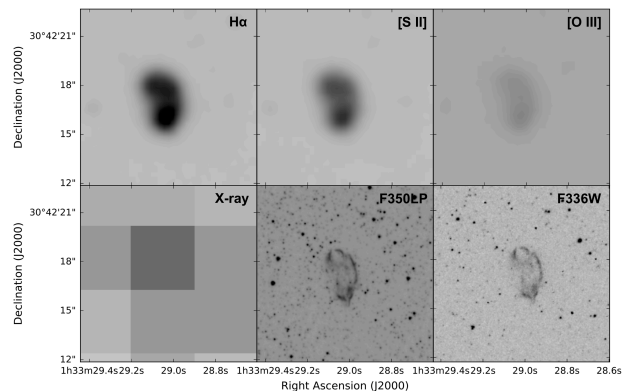


FIG. 8.— **No.184, 013329.04+304216.9 (L10-036, LL14-061)**. The *HST* images were taken with the F350LP filter in Program 13767 (PI: Trenti) and the F336W (*U*) filter in Program 14610 (PI: Dalcanton).

4.4. No.188, 013329.45+304910.7 (L10-037, LL14-062)(Figure 10)

The X-ray image of this SNR shows faint diffuse emission within a circular area with diameter of approximately 34 pc. The $H\alpha$, [S II], and [O III] images show two bright patches of emission on the eastern side of the

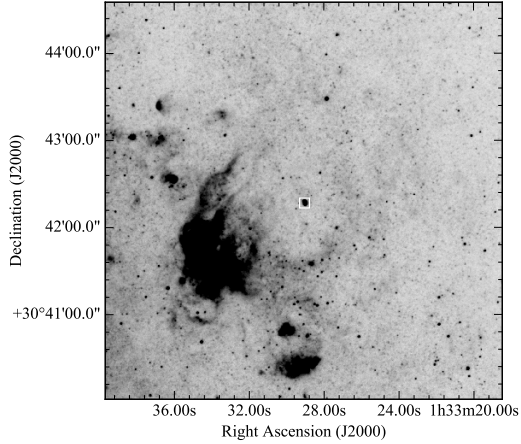


FIG. 9.— **No.184, 013329.04+304216.9 (L10-036, LL14-061)**. The $H\alpha$ image shows that this SNR is projected within a superbubble greater than 200 pc in size in NGC 595. The white box marks the location of this SNR.

SNR. The *HST* F606W and F814W images detect diffuse emission from these two patches and reveal a cluster in the southern of the two. The irregular optical morphology of this SNR and its possible association with a cluster with some ionizing power suggest that this SNR is of CC origin. Furthermore, the presence of [S II] and [O III] emission definitely rules out a Balmer-dominated Type Ia nature.

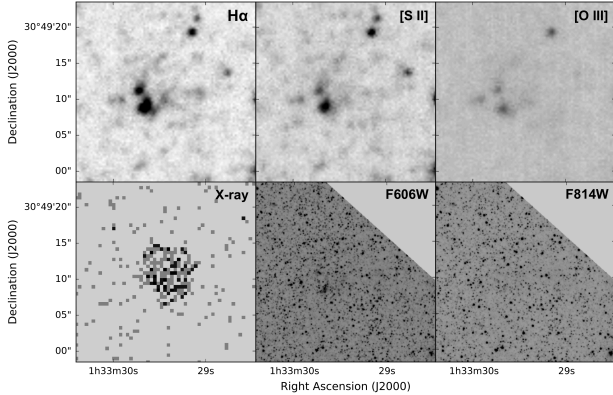


FIG. 10.— **No.188, 013329.45+304910.7 (L10-037, LL14-062)**. The *HST* images were taken with the F606W (*V*) and F814W (*I*) filters in Program 9873 (PI: Sarajedini).

4.5. *No.197, 013331.25+303333.4 (L10-039, LL14-067)*(Figure 11)

Optical counterparts of X-ray source 197 are detected in $H\alpha$, [S II], and [O III] images. A bright patch of emission is detected at the position of the X-ray source, and two fainter $H\alpha$ loops extend from the SNR location to the east. The *HST* F555W image has resolved the bright patch of emission in the SNR into four roughly parallel filaments. Furthermore, the *HST* images resolve the object projected at ~ 60 pc southeast from the SNR into a cluster. Lacking a well-defined shell structure is a characteristic often seen in CC SNRs, but not in young Type Ia SNRs in the LMC; therefore, we suggest that

the SNR associated with X-ray source 197 is a CC SNR.

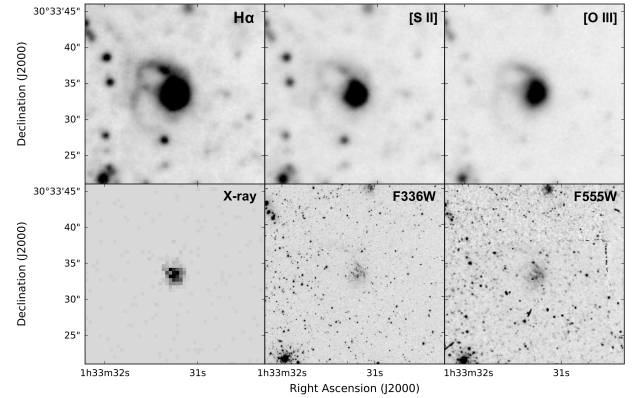


FIG. 11.— **No.197, 013331.25+303333.4 (L10-039, LL14-067)**. The *HST* images were taken with the F336W (*U*) in Program 14610 (PI: Dalcanton) the F555W (*V*) filter in Program 6038 (PI: Bianchi).

4.6. *No.236, 013335.90+303627.4 (L10-045, LL14-074)*(Figure 12)

The $H\alpha$, [S II] and [O III] images all show bright emission at the location of the X-ray source, and from this bright central region two emission loops extending to the northwest and southeast directions and fainter arcs extending to the northeast and southwest. The bright central emission is bisected by a narrow lane of lower surface brightness, and the overall morphology of the central bright emission and the two brightest loops resembles two connected chain links. The *HST* F336W and F606W images show nicely that the narrow region of low surface brightness region in the bright emission region is a dust lane. There is a star within the dust lane near the center of the bright central emission, but its photometric measurements from Massey et al. (2006, 2007, 2016) may be too contaminated by the nebular emission to be useful for spectral type estimates. The association with the dust lane and the extended ionized loop structure indicates that the SNR is most likely a CC SNR. Its [S II] and [O III] emission also rule out its being a Balmer-dominated young Type Ia SNR.

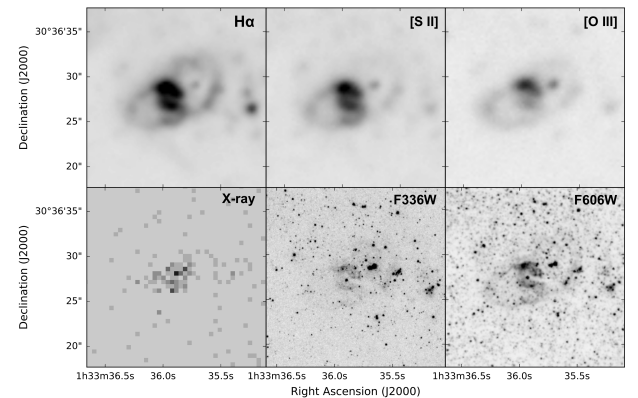


FIG. 12.— **No.236, 013335.90+303627.4 (L10-045, LL14-074)**. The *HST* images were taken with the F336W (*U*) filter in Program 14610 (PI: Dalcanton) and the F606W (*V*) filter in Program 8090 (PI: Casertano).

4.7. *No.245, 013337.08+303253.5 (L10-046, LL14-076)*(Figure 13)

This SNR is located along the prominent southern spiral arm of M33. The nearest large star-forming region is located at about 90 pc in the southeast. The SNR has a weak limb-brightening in the $H\alpha$ image, indicating a shell structure; however, there is still wide-spread diffuse emission within the shell boundary. The [S II] image shows a SNR morphology similar to that in $H\alpha$. The [O III] image shows slightly different surface brightness distribution and a less well-defined shell rim on the west side. The X-ray emission is distributed near the center of the SNR shell, as opposed to along the shell rim. This SNR is almost the largest among the nine X-ray-bright SNRs discussed in this paper, but it has the highest unabsorbed X-ray luminosity. This high unabsorbed X-ray luminosity probably results from a very high absorption correction, as this SNR has the lowest plasma temperature and the highest absorption column among the nine SNRs in Table 2. The $H\alpha$ surface brightness of this SNR is so low that its *HST* F555W and F814W images optimized to observe stars could not detect any line emission from this SNR. We are not certain whether this is a CC or Type Ia SNR. The presence of [O III] and [S II] emission indicates that this SNR is definitely not a young Balmer-dominated Type Ia SNR.

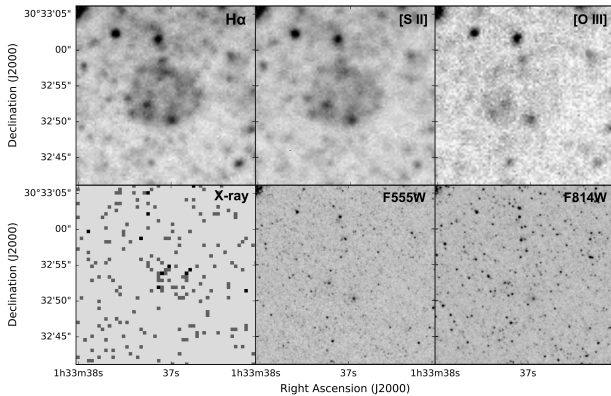


FIG. 13.— **No.245, 013337.08+303253.5 (L10-046, LL14-076)**. The *HST* images were taken with the F555W (*V*) and F814W (*I*) filters in Program 11079 (PI: Bianchi).

4.8. *No.334, 013354.91+303310.9 (L10-071, LL14-107)*(Figure 14)

The X-ray image of this SNR appears larger than the optical counterpart, but this is likely caused by the large point-spread-function of the SNR's off-axis position in the ACIS-I detector. The SNR is detected in $H\alpha$, [S II] and [O III] images. The *HST* F606W image resolves the filamentary structure of the SNR that is detected only over the western hemisphere. The strongest nebular line in the F606W band is the $H\alpha$ +[N II] line. The image in the F606W band most likely represents an $H\alpha$ image. The nebular morphology is very similar to that of the CC SNR in N4, an H II region ionized by an OB association in the LMC (Chu 1997). The SNR associated with X-ray source 334 is located only 40 pc east from a cluster that is embedded in diffuse interstellar $H\alpha$ emission (visible on the western edge of the panels in Figure 14). The

low surface brightness of the diffuse $H\alpha$ emission implies that the cluster is relatively evolved (10^7 yr or older) and has no powerful O stars left. If the SN progenitor had been ejected by this cluster, it would probably have been a B star. Based on this SNR's morphology and its interstellar and stellar environment, we suggest that it is a CC SNR.

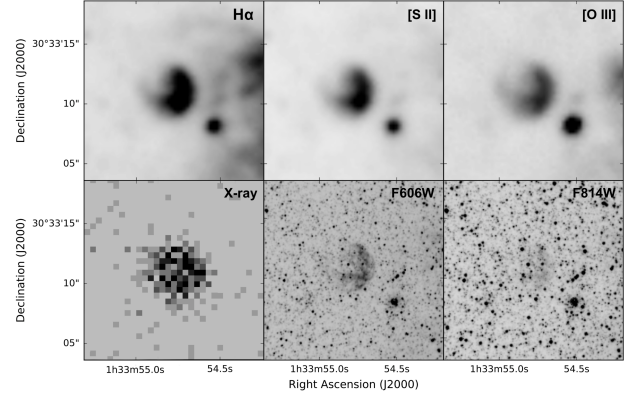


FIG. 14.— **No.334, 013354.91+303310.9 (L10-071, LL14-107)**. The *HST* images were taken with the F606W (*V*) and F814W (*I*) filters in Program 10190 (PI: Garnett).

4.9. *No.427, 013410.69+304224.0 (L10-096, LL14-140)*(Figure 15)

This SNR shows a shell structure best in the [O III] image, with a bright spot on the northwest rim (about 60° from the north). The $H\alpha$ and [S II] images show more diffuse emission in the central region, and an additional bright spot on the southeast rim, which is most likely caused by a red star that is best seen in the *HST* F814W image. The *HST* F475W image includes the $H\beta$ and [O III] line emission and thus detects the SNR shell. This high-resolution image shows a sharp shell filament in the northern rim, but much more diffuse for the rest of the shell rim. This shell morphology is very different from those of the Balmer-dominated Type Ia SNRs in the LMC. Although there are no large H II complexes in the vicinity of this SNR, a bright H II region is projected at ~ 23 pc away. We suggest that this is likely a CC SNR, and definitely not a Balmer-dominated Type Ia SNR.

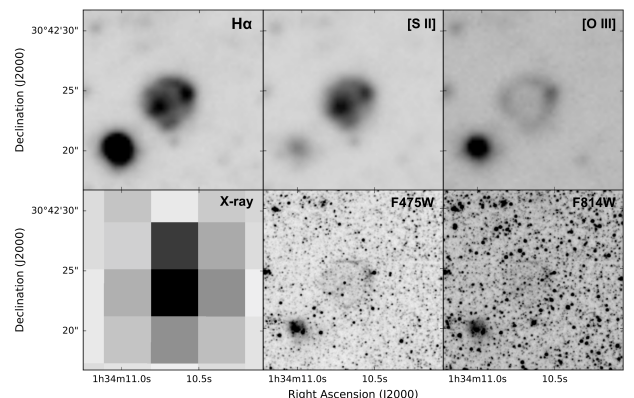


FIG. 15.— **No.427, 013410.69+304224.0 (L10-096, LL14-140)**. The *HST* images were taken with the F475W (*B*) and F814W (*I*) filters in Program 14610 (PI: Dalcanton).

5. DISCUSSION

Using the young Balmer-dominated Type Ia SNRs in the LMC as a template, we have searched M33 for similar objects. As the Type Ia SN rate is proportional to the stellar mass of a galaxy (Sullivan et al. 2006) and M33 has 2–3 times the stellar mass of the LMC (see Table 3 and references therein), we expect at least a few Balmer-dominated Type Ia SNRs in M33; however, we did not find any unambiguous candidate! This result is very puzzling. To solve this puzzle, we consider below effects of observational bias, density and ionization fraction of the ISM, Type Ia SN rate estimated from star formation history and delay time distribution (DTD), and metallicity.

5.1. Observational Bias Effect

Surveys of SNRs in the LMC have confirmed at least ~ 60 objects (Maggi et al. 2016; Bozzetto et al. 2017) and among them five are Balmer-dominated Type Ia SNRs, while surveys of SNRs in M33 have confirmed ~ 200 SNRs (Lee & Lee 2014) and zero Balmer-dominated Type Ia SNRs (this paper). The M33-to-LMC SNR number ratio, $200/60 \sim 3.3$, is not very different from their galactic stellar mass ratio, $\sim 2-3$. The size distributions of known SNRs in the LMC and M33 are shown in Figure 16. The deficiency of small SNRs in M33, especially those smaller than 10 pc in size, is a clear indication of incompleteness of SNR surveys for M33 due to the limiting angular resolution of ground-based optical observations, as 10 pc corresponds to an angular size of $2''.5$.

Our new search for young Balmer-dominated Type Ia SNRs in M33 is not subject to the size versus angular resolution effect because we use X-ray luminosity to make the initial selection of candidates. There is nevertheless a real difference in the X-ray luminosity function between M33 and the LMC. The cumulated X-ray luminosity function of M33 SNRs has been compared with that of the LMC SNRs using *XMM-Newton* and *Chandra* observations (Maggi et al. 2016; Long et al. 2010; Garofali et al. 2017). It is evident that the LMC has more X-ray-luminous SNRs than M33; for example, the LMC has 14 SNRs more luminous than 5×10^{35} ergs s^{-1} , while M33 has only nine. This difference is real and not caused by observational bias effects. It is interesting to note that among these 14 luminous LMC SNRs five are Balmer-dominated Type Ia SNRs, and among the 9 luminous M33 SNRs none is Balmer-dominated. These numbers appear to suggest that the difference between the LMC and M33 in the cumulated X-ray luminosity function is caused by an absence of luminous Balmer-dominated Type Ia SNRs in M33.

5.2. Interstellar Density Effect

M33 has a total gas mass of $\sim 1.73 \times 10^9 M_{\odot}$ and a radius of 8.2 kpc (Gratier et al. 2010), while the LMC has a total gas mass of $\sim 5.3 \times 10^8 M_{\odot}$ and a radius of 5.2 kpc (Staveley-Smith et al. 2003; Fukui et al. 2008). Assuming a similar gas scale height for M33 and the LMC, the average gas density in M33 is about 20% higher than that in the LMC. This difference in average interstellar gas densities means that X-ray emission from shocks into the ISM would be higher for Type Ia SNRs in M33 than those in the LMC. Thus, the density of the ISM cannot be responsible for the missing X-ray-bright Balmer-

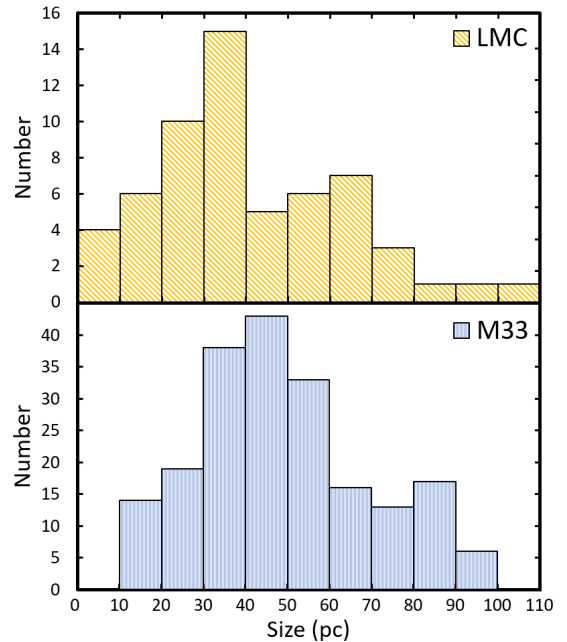


FIG. 16.— Size distributions of known SNRs in the LMC and M33. The optical sizes of the 59 known SNRs in the LMC are from Ou et al. (2018), and those of 199 known SNRs in M33 are from Lee & Lee (2014).

dominated Type Ia SNRs in M33.

5.3. Ionization Fraction of the ISM Effect

If a Type Ia SN explodes in an ionized ISM, it may not have a Balmer-dominated spectrum. The total ionizing flux available in a galaxy is proportional to the current star formation rate, which is $0.25 \pm 0.1 M_{\odot} \text{ yr}^{-1}$ for M33 and $\sim 0.21 M_{\odot} \text{ yr}^{-1}$ for (Chomiuk & Povich 2011). The total gas mass of M33 is ~ 3 times the total gas mass of the LMC. Therefore, with a high total gas mass but a comparable ionizing flux, M33 would have a larger fraction of neutral ISM, and we do not expect it to prohibit the formation of Balmer-dominated Type Ia SNRs in M33.

5.4. Type Ia SN Rate Expected from Star Formation History

For a single burst of star formation, the rate of Type Ia SNe is a function of “delay time”, the time lapse from the star formation to SN explosion. This function, called delay-time distribution (DTD) function, is expressed in a power law, $\propto t^{\alpha}$, where t is the delay time and greater than 40 Myr, and α has been determined from observations. (The DTD function is zero at $t < 40$ Myr.) For a galaxy with varying star formation rate in the past, the expected Type Ia SN rate can be derived by convolving the star formation history (SFH) with the DTD function (Maoz & Mannucci 2012). The SFH of the LMC has been determined by Harris & Zaritsky (2009) and the SFH of M33 has been determined by (Javadi et al. 2017), as shown in Figure 17, where star formation rates (SFR) are plotted as a function of look-back time. We have interpolated each SFH to obtain a continuous function of t for SFR and convolved it with a DTD function using $\alpha \sim -1.07$ and the Hubble-time-integrated SN Ia production efficiency of 1.3 ± 0.1 Type Ia SN per 1000

TABLE 3
COMPARISON BETWEEN THE LMC AND M33

	Units	LMC	M33	References of LMC	References of M33
Total Baryonic Mass	M_{\odot}	3.2×10^9	$6.2\text{--}9.2 \times 10^9$	van der Marel et al. (2002)	Corbelli (2003)
HI mass	M_{\odot}	$(4.8 \pm 0.2) \times 10^8$	1.4×10^9	Staveley-Smith et al. (2003)	Gratier et al. (2010)
H ₂ mass (CO line)	M_{\odot}	$\sim 5 \times 10^7$	3.3×10^8	Fukui et al. (2008)	Gratier et al. (2010)
Total gas mass	M_{\odot}	$\sim 5.3 \times 10^8$	1.73×10^9
Recent SFR	$M_{\odot} \text{ yr}^{-1}$	0.21	0.25	Chomiuk & Povich (2011)	Chomiuk & Povich (2011)
Total SNRs		59	199	Maggi et al. (2016)	Lee & Lee (2014)
Confirmed Balmer-dominated SNRs		5	0	Ou et al. (2018)	this paper

M_{\odot} of formed stellar mass determined by Maoz & Graur (2017). The resulting Type Ia SN rates of the LMC and M33 are plotted in Figure 18. Given the SFH of the LMC and M33, we expect M33 to have 50% more Type Ia SNRs than the LMC; however, we did not detect any X-ray-bright Type Ia SNRs in M33.

5.5. Metallicity Effect

The metallicity of a galaxy affects Balmer-dominated Type Ia SNRs in two respects. First, the Type Ia SN rate of a galaxy depends on metallicity, Z (Kistler et al. 2013). The rate is proportional to $Z^{-0.3}$ to $Z^{-0.5}$ for single-degenerate SNe and $Z^{-0.4}$ for double-degenerate SNe. The stellar abundances of M33 have a bimodal distribution, with $[\text{Fe}/\text{H}]$ peaking near -1.3 and -1.7 , while the distribution of LMC stellar abundances peaks at $[\text{Fe}/\text{H}] \sim -1.15$ (Cioni 2009). We can adopt an approximate metallicity dependence of $Z^{-0.4}$ for the Type Ia SN rate. For the stellar masses and metallicities of M33 and the LMC, the Type Ia SN rate of M33 should be at least ~ 3 times as high as the LMC. This metallicity effect does not solve the puzzle of not detecting X-ray-bright Balmer-dominated Type Ia SNRs in M33.

The second metallicity effect is on the X-ray emissivity that is directly proportional to the metal content of the plasma. X-ray emission from a young Type Ia SNR can originate from the forward shocks into ISM and the reverse shocks into the SN ejecta. The abundance of the SN ejecta is determined by the nucleosynthesis in the SN explosion and depends on the SN explosion mechanism. Without a priori knowledge of the differences in Type Ia SN populations between M33 and the LMC, we assume the Type Ia SN ejecta abundances are similar between M33 and the LMC. The X-ray emission associated with the forward shocks is from shocked ISM. The oxygen abundance $12+\log(\text{O}/\text{H})$ of M33 is in the range of 8.1 to 8.5 (Rosolowsky, & Simon 2008), while the LMC has ~ 8.35 (Russell, & Dopita 1992). Within a factor of 2, the interstellar abundances of M33 and the LMC are very similar. There is no indication that the metallicities of M33 and the LMC are different enough to cause large differences in the X-ray emissivity of Type Ia SNRs.

6. SUMMARY AND CONCLUSION

Conventional surveys of SNRs using $[\text{S II}]/\text{H}\alpha$ ratios as diagnostics would miss the young Balmer-dominated Type Ia SNRs. We have thus applied a new methodology to search for Balmer-dominated Type Ia SNRs in M33: using $L_X \geq 5 \times 10^{35} \text{ ergs s}^{-1}$ to select thermal X-ray sources, examining their optical counterparts in $\text{H}\alpha$, and checking whether they are detected in $[\text{S II}]$ and $[\text{O III}]$

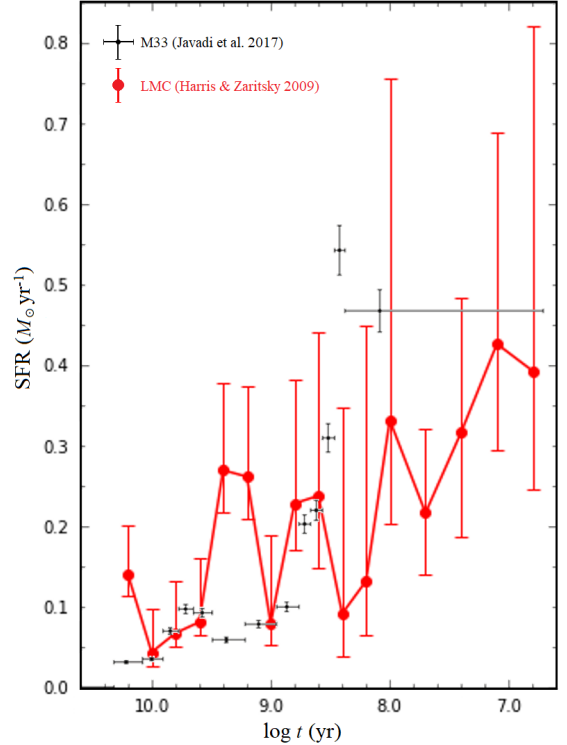


FIG. 17.— Star formation history of the LMC and M33. The SFH of the LMC is from Harris & Zaritsky (2009) and the SFH of M33 is from Javadi et al. (2017).

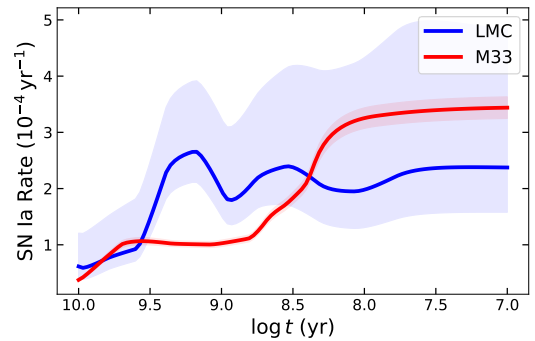


FIG. 18.— Expected Type Ia SN rates for the LMC and M33.

images. While there are nine known SNRs in M33 that meet the X-ray luminosity criterion, none of them are Balmer-dominated.

The LMC hosts five Balmer-dominated Type Ia SNRs, and all of them have X-ray luminosities greater than $8 \times 10^{35} \text{ ergs s}^{-1}$ and thermal X-ray emission. Among

the five smallest known Type Ia SNRs in the Galaxy, the Tycho and Kepler SNRs have X-ray properties similar to those in the LMC, while G1.9+0.3, SN1006, and RCW86 have X-ray luminosities lower than 5×10^{35} ergs s⁻¹ and show nonthermal X-ray emission. Our X-ray luminosity selection criterion for Balmer-dominated SNRs in M33 aims at the X-ray-bright SNRs similar to those in the LMC or Kepler and Tycho in the Galaxy.

The absence of X-ray-bright Balmer-dominated Type Ia SNRs in M33 is surprising, because M33's stellar mass is 2–3 times the LMC's mass and we expect at least a few X-ray-bright Balmer-dominated Type Ia SNRs in M33. We have computed the Type Ia SN rates expected from the SFH and SN Ia DTD function, and find that Type Ia SN rate of M33 should be 1.5 times that of the LMC, contrary to what we have found. We have also considered

observational biases, interstellar densities and ionization conditions, and metallicity effects, but none of these effects can explain the absence of X-ray-bright Balmer-dominated Type Ia SNRs in M33.

It is intriguing that the Galaxy, LMC, and M33 exhibit different Type Ia SNR population – The Galaxy has both X-ray-bright and X-ray-faint Type Ia SNRs, the LMC does not have the X-ray-faint ones, while M33 does not have the X-ray-bright ones.

We are very thankful to the anonymous reviewer who has made very useful comments and suggestions to improve this paper. This research is supported by grants MOST 107-2119-M-001-018 and MOST 108-2112-M-001-045 from the Ministry of Science and Technology of Taiwan, Republic of China.

REFERENCES

- Allen, M. G., Groves, B. A., Dopita, M. A., et al. 2008, *ApJS*, 178, 20
- Badenes, C., Borkowski, K. J., Hughes, J. P., et al. 2006, *ApJ*, 645, 1373
- Badenes, C., Hughes, J. P., Bravo, E., et al. 2007, *ApJ*, 662, 472
- Badenes, C., Hughes, J. P., Cassam-Chenaï, G., et al. 2008, *ApJ*, 680, 1149
- Bourgés, L., Lafrasse, S., Mella, G., et al. 2014, *Astronomical Data Analysis Software and Systems XXIII*, 223
- Bozzetto, L. M., Filipović, M. D., Vukotić, B., et al. 2017, *ApJS*, 230, 2
- Chevalier, R. A., Kirshner, R. P., & Raymond, J. C. 1980, *ApJ*, 235, 186
- Chomiuk, L. & Povich, M. S. 2011, *AJ*, 142, 197
- Chu, Y.-H. 1997, *AJ*, 113, 1815
- Cioni, M.-R. L. 2009, *A&A*, 506, 1137
- Corbelli, E. 2003, *MNRAS*, 342, 199
- Cutri, R. M., Skrutskie, M. F., van Dyk, S., et al. 2003, *VizieR Online Data Catalog*, II/246
- Edwards, Z. I., Pagnotta, A., & Schaefer, B. E. 2012, *ApJ*, 747, L19
- Fleming, T. A., Schmitt, J. H. M. M., & Giampapa, M. S. 1995, *ApJ*, 450, 401
- Freedman, W. L., Madore, B. F., Gibson, B. K., et al. 2001, *ApJ*, 553, 47
- Fukui, Y., Kawamura, A., Minamidani, T., et al. 2008, *ApJS*, 178, 56
- Gaetz, T. J., Blair, W. P., Hughes, J. P., et al. 2007, *ApJ*, 663, 234
- Gaia Collaboration, Brown, A. G. A., Vallenari, A., et al. 2018, *A&A*, 616, A1
- Garofali, K., Williams, B. F., Plucinsky, P. P., et al. 2017, *MNRAS*, 472, 308
- González Hernández, J. I., Ruiz-Lapuente, P., Filippenko, A. V., et al. 2009, *ApJ*, 691, 1
- González Hernández, J. I., Ruiz-Lapuente, P., Tabernero, H. M., et al. 2012, *Nature*, 489, 533
- Gordon, S. M., Kirshner, R. P., Long, K. S., Blair, W. P., Duric, N., & Smith, R. C. 1998, *ApJS*, 117, 89 [G98]
- Gratier, P., Braine, J., Rodriguez-Fernandez, N. J., et al. 2010, *A&A*, 522, A3
- Hachisu, I., Kato, M., & Nomoto, K. 2008, *ApJ*, 679, 1390
- Harris, J., & Zaritsky, D. 2009, *AJ*, 138, 1243
- Hughes, J. P., Hayashi, I., Helfand, D., et al. 1995, *ApJ*, 444, L81
- Ivanov, G. A. 2008, *Kinematika i Fizika Nebesnykh Tel*, 24, 480
- Javadi, A., van Loon, J. T., Khosroshahi, H. G., et al. 2017, *MNRAS*, 464, 2103
- Kerzendorf, W. E., Childress, M., Schwarwächter, J., Do, T., & Schmidt, B. P. 2014, *ApJ*, 782, 27
- Kerzendorf, W. E., Yong, D., Schmidt, B. P., et al. 2013, *ApJ*, 774, 99
- Kerzendorf, W. E., Strampelli, G., Shen, K. J., et al. 2018, *MNRAS*, 479, 192
- Kistler, M. D., Stanek, K. Z., Kochanek, C. S., Prieto, J. L., & Thompson, T. A. 2013, *ApJ*, 770, 88
- Koyama, K., Petre, R., Gotthelf, E. V., et al. 1995, *Nature*, 378, 255
- Krause, O., Tanaka, M., Usuda, T., et al. 2008, *Nature*, 456, 617
- Lee, J. H., & Lee, M. G. 2014, *ApJ*, 793, 134 [LL14]
- Lewis, K. T., Burrows, D. N., Hughes, J. P., et al. 2003, *ApJ*, 582, 770
- Li, C.-J., Chu Y.-H., & Gruendl, R. A. et al. 2017, *ApJ*, 836, 35
- Li, C.-J., Kerzendorf, W. E., Chu, Y.-H., et al. 2019, *ApJ*, 886, 99
- Litke, K. C., Chu, Y.-H., Holmes, A., et al. 2017, *ApJ*, 837, 111
- Long, K. S., Charles, P. A., Blair, W. P., & Gordon, S. M. 1996, *ApJ*, 466, 750
- Long, K. S., Blair, W. P., Winkler, P. F., et al. 2010, *ApJS*, 187, 495 [L10]
- Nomoto, K. 1982, *ApJ*, 257, 780
- Maggi, P., Haberl, F., Kavanagh, P. J., et al. 2016, *A&A*, 585, A162
- Maoz, D., & Graur, O. 2017, *ApJ*, 848, 25
- Maoz, D., & Mannucci, F. 2012, *PASA*, 29, 447
- Massey, P., Olsen, K. A. G., Hodge, P. W., et al. 2006, *AJ*, 131, 2478
- Massey, P., McNeill, R. T., Olsen, K. A. G., et al. 2007, *AJ*, 134, 2474
- Massey, P., Neugent, K. F., & Smart, B. M. 2016, *AJ*, 152, 62
- Matonick, D. M., & Fesen, R. A. 1997, *ApJS*, 112, 49
- Ou, P.-S., Chu, Y.-H., Maggi, P., et al. 2018, *ApJ*, 863, 137
- Pagnotta, A., & Schaefer, B. E. 2015, *ApJ*, 799, 101
- Pecaut, M. J., & Mamajek, E. E. 2013, *ApJS*, 208, 9
- Qi, Z., Yu, Y., Bucciarelli, B., et al. 2015, *AJ*, 150, 137
- Rest, A., Matheson, T., Blondin, S., et al. 2008, *ApJ*, 680, 1137
- Reynolds, S. P., Borkowski, K. J., Green, D. A., et al. 2008, *ApJ*, 680, L41
- Rosolowsky, E., & Simon, J. D. 2008, *ApJ*, 675, 1213
- Ruiz-Lapuente, P., Comeron, F., Méndez, J., et al. 2004, *Nature*, 431, 1069
- Ruiz-Lapuente, P., Damiani, F., Bedin, L., et al. 2018, *ApJ*, 862, 124
- Russell, S. C., & Dopita, M. A. 1992, *ApJ*, 384, 508
- Sabbadin, F., & Bianchini, A. 1979, *PASP*, 91, 62
- Schaefer, B. E., & Pagnotta, A. 2012, *Nature*, 481, 164
- Staveley-Smith, L., Kim, S., Calabretta, M. R., Haynes, R. F., & Kesteven, M. J. 2003, *MNRAS*, 339, 87
- Sullivan, M., Le Borgne, D., Pritchett, C. J., et al. 2006, *ApJ*, 648, 868
- Tuohy, I. R., Dopita, M. A., Mathewson, D. S., Long, K. S., & Helfand, D. J. 1982, *ApJ*, 261, 473
- Tüllmann, R., Gaetz, T. J., Plucinsky, P. P., et al. 2011, *ApJS*, 193, 31
- van der Marel, R. P., Alves, D. R., Hardy, E., & Suntzeff, N. B. 2002, *AJ*, 124, 2639
- Webbink, R. F. 1984, *ApJ*, 277, 355
- Whelan, J., & Iben, I., Jr. 1973, *ApJ*, 186, 1007
- Williams, B. J., Blair, W. P., Blondin, J. M., et al. 2011, *ApJ*, 741, 96
- Woods, T. E., Ghavamian, P., Badenes, C., et al. 2018, *ApJ*, 863, 120
- Zacharias, N., Monet, D. G., Levine, S. E., et al. 2004, *American Astronomical Society Meeting Abstracts* 205, 48.15
- Zickgraf, F.-J., Krautter, J., Reffert, S., et al. 2005, *A&A*, 433, 151